Synthesis and characterization of Ce and Er doped ZrO$_2$ nanoparticles as solar light driven photocatalysts

Chiara Gionco[a], Simelys Hernández[*b], Micaela Castellino[c], Tanveer Ahmed Gadhi[b,d], José Alejandro Muñoz-Tabares[c], Erik Cerrato[a], Alberto Tagliaferro[b,e], Nunzio Russo[b], Maria Cristina Paganini[*a]

*corresponding authors: mariacristina.paganini@unito.it, simelys.hernandez@polito.it

[a] Department of Chemistry, University of Torino, Via Giuria 7, 10125, Turin, Italy
[b] Department of Applied Science and Technology, DISAT, Politecnico di Torino, 10129, Turin, Italy
[c] Center for Sustainable Future Technologies, CSFT, IIT@Polito, Istituto Italiano di Tecnologia, Corso Trento 21, 10129, Turin, Italy
[d] U.S. Pakistan Center for Advanced Studies in Water (USPCAS-W), Mehran University of Engineering and Technology, Jamshoro 76062, Pakistan.
[e] Faculty of Science, University of Ontario Institute of Technology, Oshawa (ON), Canada

Abstract

In this work, nanostructured rare-earth-doped zirconia was successfully synthesized, through a simple hydrothermal method, with a rare-earth oxide (REO)-based content varying from 0.5 to 5% molar (REO = CeO$_2$; Er$_2$O$_3$). The samples were characterized by using several techniques, such as X-ray diffraction, transmission electron microscopy, X-ray photoelectron spectroscopy, diffuse reflectance spectroscopy. The photoactivity of the samples was tested under irradiation with simulated solar light by both the spin trapping technique, using DMPO (5,5-dimethyl-1-pyrroline-N-oxide) as spin trapping agent, and by the photodegradation of Rhodamine B, a common textile dye. All the doped samples resulted more active than the bare zirconia, and the correlation between the physical-chemical properties and the photoactivity of the materials has been investigated.

Key words:

Rare earth alloys and compounds; Rhodamine B; Third-generation photocatalysts; Dye degradation, oxide materials, electronic band structure

1. Introduction

Long-term climate objective of European Union (EU) and most of developed countries as a group is to reduce greenhouse gas (GHG) emissions by 80-95% in 2050 compared to 1990. Current policies aim at achieving a more sustainable economy and energy system, which may reduce costs and avoid damages in the longer run [1]. In such context, safeguard of water resource and an efficient exploitation of renewable energy sources is of fundamental importance for the future of humankind. Thus, extensive research and development (R&D) efforts are in progress to exploit the enormous amount of solar power that falls on our planet (100.000 TW). Among them, the improvement of sun-driven photo-catalytic conversion technologies have been growing during the last decade and is currently a hot R&D topic in both solar fuels production and advanced oxidation process fields.

In this context, advanced oxidation processes (AOPs) are powerful emerging technologies for the abatement of organic molecules in air or aqueous systems, based on the generation of very reactive species such as hydroxyl radicals ($^{\bullet}OH$) able to oxidize a broad range of pollutants quickly and non-selectively [2]. In particular, purification of wastewater coming from textile industries is a great issue because up to 20% of the total world dye production is released in such effluents. Textile dyes constitute one of the largest group of organic compounds with severe environmental danger, because they are a considerable source of non-aesthetic pollution and eutrophication and can moreover originate dangerous byproducts [3]. Hence, in contrast to the traditional non-destructive decolorization physical techniques (*i.e.* adsorption, ultrafiltration, reverse osmosis, coagulation by chemical agents, etc.), the development of highly efficient and low-cost photo-catalysts-based AOP could allow to deal with the problem of complete destruction of organic molecules in water purification processes [4].

Since the first demonstrations of photoelectrochemical water splitting [5], titanium dioxide (TiO_2), which is the main player of the so-called first generation of photoactive materials, has been the most commonly studied photocatalyst for that reaction and for other photocatalytic environmental applications [6, 7]. However, it is known that pure TiO_2 is efficient only under UV light irradiation (due to its high band gap of around 3.2 eV) and it is poorly effective under sunlight, which prevalently contains visible and near-infrared (NIR) radiations. In the past 20 years, researchers have mainly focused on other low-cost and abundant metal oxides (*i.e.* $BiVO_4$, WO_3) [8, 9] able to absorb visible light; or on the modification of high band gap materials such as TiO_2 or ZnO, by means of doping with transition-metal or non-metal ions [10], ion implantation, dye sensitization [11], or through the formation of hybrid nanostructures [12, 13]. All of these systems are part of the so-called second-generation photoactive materials [6]. Recently ceria and CeO_2-containing materials have been investigated and employed in heterogeneous catalysis. The antioxidant activity of ceria seems to be due to its ability in scavenging free radicals ($OH^{\bullet}$) which is also related to the ability of ceria to switch between Ce^{4+}/Ce^{3+} oxidation states [14, 15] . In order to improve the photocatalytic activity of CeO_2 under visible light or solar irradiation, one of the most efficient method is the doping with other metallic oxides. It has been reported the catalytic degradation of Rhodamine B (RhB), a fluorescent dye, employed as a model reaction to evaluate the catalytic activity of the cerium based doped materials. [16]

In the past five years, a third-generation of novel photoactive materials has emerged, which is based on the band gap engineering of high band gap oxides. For instance, zirconium dioxide (ZrO_2), a ceramic material also used as heterogeneous catalysts, has found only few applications in photocatalysis [17-20] because of its large band gap (ca. 5.0 eV), a value that allows to absorb only

a negligible fraction of the solar light impinging on the earth surface. Nevertheless, the high redox potentials of the photo-generated e^-/h^+ pairs on this material, together with its good chemical and optical stability, environmental and biological compatibility as well as its low-cost, render the ZrO_2 suitable for several photocatalytic reactions. Therefore, ZrO_2 has been modified with the aim to achieve charges separation and photocatalytic reactions by using low energy photons belonging to the visible light spectra. For example, tiny concentrations of rare-earths (*e.g.* Ce, Y, Eu, Tb, Sm, Er) [21-23], transition-metal ions (*e.g.* Fe) [24] and non-metal dopants (*e.g.* C, N) [25, 26] have been incorporated into ZrO_2 powders and have demonstrated photocatalytic activity under visible light irradiation for abatement of different dyes (*e.g.* methylene blue). Nevertheless, a full understanding of both the role of such dopants on the modification of the physical and chemical properties of ZrO_2 and how they influence the photocatalytic activity of this high band gap material have not yet been fully investigated.

In this work, Ce and Er doped ZrO_2 nanoparticles were synthesized with different concentrations of dopants by an optimized hydrothermal method [22, 23]. The photocatalytic activity of the doped-ZrO_2 powders was investigated for the degradation of a cationic dye, Rhodamine B, and correlated with the physico-chemical and optical properties of these materials which were evaluated by XRD, UV-Vis spectroscopy, TEM, XPS and EPR analyses. The final outcome of this work is to give insights into the role of rare-earth dopants on the visible light driven photocatalytic performance of ZrO_2-based materials, for driving future developments of this third generation photocatalyst.

2. Materials and methods

2.1. Preparation of the doped ZrO_2 materials

Various photocatalytic materials based on zirconia doped with rare earth ions (RE, RE=Ce, Er) were prepared employing reactants purchased from Aldrich, used without any further purification treatment.

A hydrothermal process has been used for the synthesis of the photocatalysts, starting from a 1.0 M aqueous solution containing, in the stoichiometric ratio, $ZrOCl_2 \cdot 8H_2O$ and $Ce(SO_4)_2$ or $Er(NO_3)_3 \cdot 5H_2O$. The pH of the solution was then adjusted to 11 using a 4.0 M NaOH aqueous solution inducing the formation of a gel. The gel was then transferred into a 125 ml Teflon-lined stainless-steel autoclave, 70% filled, which was heated in oven at 175 °C for 15 hours. The precipitates were then centrifuged and washed three times with de-ionized water, then dried at 60°C. For comparison purposes, pure ZrO_2 was prepared with the same procedure, without the presence of the RE dopant. Finally, the prepared powders were calcined at 500 °C for 2 hours.

For each dopant (Ce or Er), samples having different RE content, on an oxide basis, namely 0.5%, 1% and 5% molar, were prepared. Samples will be labeled using Z for zirconia, C for cerium oxide and E for erbium oxide, followed by figures indicating the molar percentage of the dopant oxide. For example, Z means bare zirconia while CZ05 and EZ1 indicate materials containing 0.5 % of cerium oxide and 1 % of erbium oxide respectively.

2.2. Characterization

X-Ray Diffraction (XRD) patterns were recorded with a PANalytical PW3040/60 X'Pert PRO MPD using a copper Kα radiation source (0.15418 nm) and a Bragg Brentano geometry. X'Pert High-Score software was used for data handling. Rietveld refinement was performed on the

diffraction patterns to determine the crystallite size and relative abundance of phases, using the MAUD 2.26 software [27] and a NIST Si powder to determine the instrumental function.

The morphology and aggregation state of the photocatalysts were evaluated by using a field emission scanning electronic microscope (FESEM, Zeiss Merlin)

In addition, both morphology and crystalline structure of the ZrO_2 samples were characterized by means of transmission electron microscopy (TEM) made with a FEI Tecnai F20ST operating at 200 kV. For the TEM analyses, the powders were dispersed in ethanol (purity > 99.8 %, Sigma-Aldrich) by sonication for 5 min and then placed on a TEM grid.

A PHI 5000 Versaprobe Scanning X-ray Photoelectron Spectrometer (monochromatic Al Kα X-ray source with 1486.6 eV energy), was employed to check the material surface chemistry. High resolution (Pass energy: 23.5 eV) and survey spectra (Pass energy: 187.85 eV) were collected using a beam size of 100 μm. A combination of an electron gun and an Ar ion gun was used as neutralizer system to compensate the positive charging effect during the measurement. Fitting procedure and deconvolution analyses were done using the Multipak 9.6 dedicated software. All core level peak energies were referenced to C1s peak at 284.5 eV (C-C/C-H sp2 bonds).

Diffuse Reflectance Spectroscopy (DRS) data were recorded using a Varian Cary 5000 spectrometer, coupled with an integration sphere for diffuse reflectance studies, using a Carywin-UV/scan software. A sample of PTFE with 100% reflectance was used as reference.

The generation of radical species in solution was monitored by the Electron Paramagnetic Resonance (EPR) spectroscopy (spin trapping technique) using a Miniscope 100 spectrometer from Magnettech and DMPO (5,5-dimethyl-1-pyrroline-N-oxide, Alexis Biochemicals, San Diego, CA) as spin trapping agent. In a typical experiment 28 mg of powder were suspended in 1 ml of water. Then 250 μl of a 0.17M DMPO solution were added and the irradiation started. The irradiation was performed with a 500 W Xenon lamp (Oriel Instruments) equipped with an IR water filter. A 400 nm cut-off filter was used to eliminate the UV radiation. The generation of radicals versus time was monitored by taking every time 50 μl of solution for the measure.

2.3. Dye Photodegradation

The photocatalytic activity of doped and undoped samples was evaluated by investigating the degradation of rhodamine B (*RhB*) dye under cold light emitting halogen lamp (solar spectrum) Flexilux-650 at very small irradiance (40 Wm^{-2}) by using 15 mL of the dye solution with a dye concentration of 10 mg/L. The powder loaded in the dye solution was 10 mg and the suspension was stirred for 60 min in the dark to allow the system to reach adsorption-desorption equilibrium. An aliquot of 3 mL was taken from the suspension at different irradiation time centrifuged at 5000 rpm for 5 min and analyzed to record absorbance spectra using UV-vis spectrophotometer (Agilent Cary 60 UV-Vis); after each analysis aliquot were returned to the vial to preserve the same amount of photocatalyst and extracted solution. The total organic carbon (TOC) analysis of the irradiated dye solution was investigated by using an automated total organic carbon analyzer (TOC-V, Shimadzu, Japan) to confirm the dye mineralization.

3. Results

3.1. Structural and optical characterization

Figure 1 shows the XRD patterns obtained for the pure zirconia sample and the Ce doped ZrO_2 samples. The patterns obtained for the Er doped ZrO_2 samples are very similar to the Ce doped ones

and are reported in the Supplementary Information (Figure S1). The XRD pattern show that the samples are all crystalline and constituted by a mixture of two ZrO_2 polymorphs: tetragonal (t-ZrO_2) and monoclinic (m-ZrO_2). The percentage of the tetragonal phase in the samples rises by increasing the dopant amount, and the samples containing 5% of REO are mainly constituted by t-ZrO_2 (see also Table 1). On the patterns we performed a Rietveld refinement using the MAUD software [27], whose results are reported in Table 1. The cell parameters of the m-ZrO_2 phase are poorly influenced by the insertion of the dopant, while the t-ZrO_2 register an increasing distortion with increasing RE content.
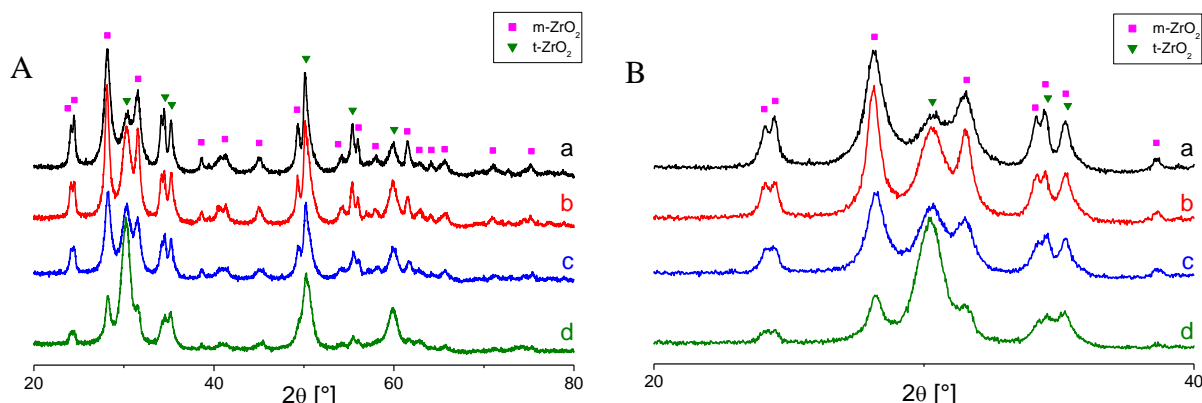

Figure 1. XRD patterns of pure ZrO_2 (a, black) and CeO_2-doped ZrO_2 with increasing concentration of CeO_2: 0.5%mol (b, red), 1%mol (c, blue) and 5%mol (d, green). Panel A is the full pattern, panel B shows a magnification in the range 20-40° of 2θ.

Moreover, as it can be seen from the enlargement in Figure 1B, the m-ZrO_2, both in the bare oxide and in the doped materials, present some degree of anisotropy. Indeed, for the same phase (m-ZrO_2, identified by the magenta squares) the XRD peaks do not present the same broadening (e.g. the first two peaks are narrower than the following two).

Indeed, the peaks broadening is not constant, but varies along with the different plan families. For this reason, the Popa model [28] was used for the refinement of this phase. The maximum (D) and minimum (d) crystallite sizes obtained from the Rietveld refinement along the [1 1 0] and [-1 1 1] planes, respectively, are listed in Table 1. Figure S2 reports the crystallite shape obtained from the MAUD software for m-ZrO_2 of the CZ05 and EZ05 samples.

Table 1. Cell parameters, weight percentage and crystallite size obtained from Rietveld refinement of XRD patterns; a, b and c are the lattice parameters, β is the angle between a and c axes for the monoclinic cell, %wt is the weight percentage of a given phase, d is the crystallite size for t-ZrO_2. D and d are the maximum and minimum crystallite sizes for the anisotropic m-ZrO_2. XPS deconvolution parameters for the Zr3d$_{5/2}$ peak.

| Sample | XRD | | | | | | | | XPS Zr 3d$_{5/2}$ | | |
	Phase	%wt	a [Å]	b [Å]	c [Å]	β [°]	d [nm]	D [nm]	Phase[a]	BE [eV]	%
Z	t-ZrO_2	34%	3.58		5.23		7		ZrO_x/t-ZrO_2	181.5	76.6
	m-ZrO_2	66%	5.18	5.22	5.34	99.59	9	43	m-ZrO_2	182.2	23.4
EZ05	t-ZrO_2	48%	3.62		5.17		11		ZrO_x/t-ZrO_2	181.2	48.4
	m-ZrO_2	52%	5.18	5.22	5.35	99.67	14	34	m-ZrO_2	181.8	51.6
EZ1	t-ZrO_2	44%	3.63		5. 16		10		ZrO_x/t-ZrO_2	180.8	31.6
	m-ZrO_2	56%	5.19	5.22	5. 34	99.55	10	47	m-ZrO_2	182.1	68.4
EZ5	t-ZrO_2	72%	3.64		5. 16		12		ZrO_x/t-ZrO_2	181.1	54.7
	m-ZrO_2	28%	5.18	5.22	5. 35	99.58	12	63	m-ZrO_2	182.1	45.3

5

CZ05	t- ZrO_2	39%	3.62		5.16		10		ZrO_x/t-ZrO_2	180.9	40.5
	m- ZrO_2	61%	5.19	5.22	5.35	99.71	13	40	m-ZrO_2	182.1	59.5
CZ1	t- ZrO_2	41%	3.64		5.11		9		ZrO_x/t-ZrO_2	180.9	63.7
	m- ZrO_2	59%	5.18	5.21	5.34	99.42	11	45	m-ZrO_2	181.9	36.3
CZ5	t- ZrO_2	68%	3.64		5.13		11		ZrO_x/t-ZrO_2	181.1	54.6
	m- ZrO_2	32%	5.18	5.21	5.34	99.45	12	37	m-ZrO_2	181.9	45.4

[a] The lower binding energy shift has been assigned to the sub-oxide/tetragonal phase, while the higher binding energy shift has been attributed to the monoclinic stoichiometric ZrO_2, according to the literature.

The morphology and the aggregation state of the materials were evaluated with a field emission scanning electronic microscope (FESEM) and the images are reported in Figure S3 (SI). All the samples present a morphology typical of aggregated, nanometric sized, powders. The pure zirconia shows the presence of "rice-like" structures, with a lateral dimension of less than 100nm. For both Ce and Er dopants, the shape of the nanometric structures becomes more spherical and smaller increasing the RE content.

For a further insight, the morphology and crystalline structure of the powders were also investigated through TEM. Figure 2 reports the images obtained at low (first column) and high (second and third columns) magnification for pure and doped (0.5 and 5% molar concentration) samples. The analysis revealed that all samples present two different grain morphologies: homogeneous nanocrystallites approximately 10 nm in diameter and grains close to 100 nm in diameter. The high-resolution (HRTEM) images allowed us to study these grains in deep. The nanocrystallites correspond to a mix of tetragonal and monoclinic ZrO_2, as evidenced by both the selected area electron diffraction (SAED) patterns and the interplanar distances of the HRTEM images. The bigger grains, on the other hand, show the presence of the monoclinic phase alone. In addition, many of them present the twins (i and ii in Figure 2A, 2B and 2C) characteristic of the tetragonal to monoclinic martensitic transformation. The samples with low dopant concentration (0.5%, Figures 2 B and C, 1% not reported for sake of brevity) show a morphology very similar to that of pure ZrO_2, but the twinned grains have a relatively lower size (60 nm instead of 100 nm). The morphology of the samples containing a higher amount of RE (5%, Figures 2D and E), on the other hand, is quite different. As expected from the XRD results, the nanocrystals in these samples are mainly due to the tetragonal phase. Moreover, the large grains, that are less common, are not twinned, indicating a nucleation of the monoclinic phase rather than the martensitic transformation. None of the analyzed samples, showed the presence of phases different from zirconia, in agreement with the XRD results. This fact, was further confirmed by the STEM-EDS maps reported in Figure S4. All the maps evidence a uniform distribution of both Ce and Er dopants, without any segregation of RE related phases.

Further information about the chemical composition and the crystallographic phase identification were provided by XPS characterization. The analysis was performed on bare ZrO_2 powder together with the two oxide dopants, for all the precursor concentrations. From the Zr3d doublet analysis (see Figure 3 A-C) it was possible to distinguish between two oxidation states: a first one at lower binding energy, which is attributed to sub-oxide or tetragonal phase [29], and a second one due to stoichiometric and monoclinic ZrO_2 [30]. The deconvolution procedures, not reported in the Figure, has provided the value reported in Table 1. For sample CZ05H a third doublet (184.1 and 186.5 eV) has been introduced in order to fit properly the experimental data. This chemical shift has been assigned to the 3d transition reported for tetragonal ZrO_2 by A. Barrera et al.[31]. As it can be seen there is not a clear trend in the phase concentration according to the presence of the oxides doping, comparing these XPS data with the XRD one. This may be due to the fact that on the surface the

concentration of defects and dangling bonds is higher, especially for the monoclinic phase, as reported by S. Ardizzone et al. [32], so XPS is more sensitive to these non-crystalline structures. Even though m-ZrO_2 is the stable bulk phase below 1300 K, the t-ZrO_2 phase can be thermodynamically preferred in nano-sized systems because of its relatively low surface energy [33].
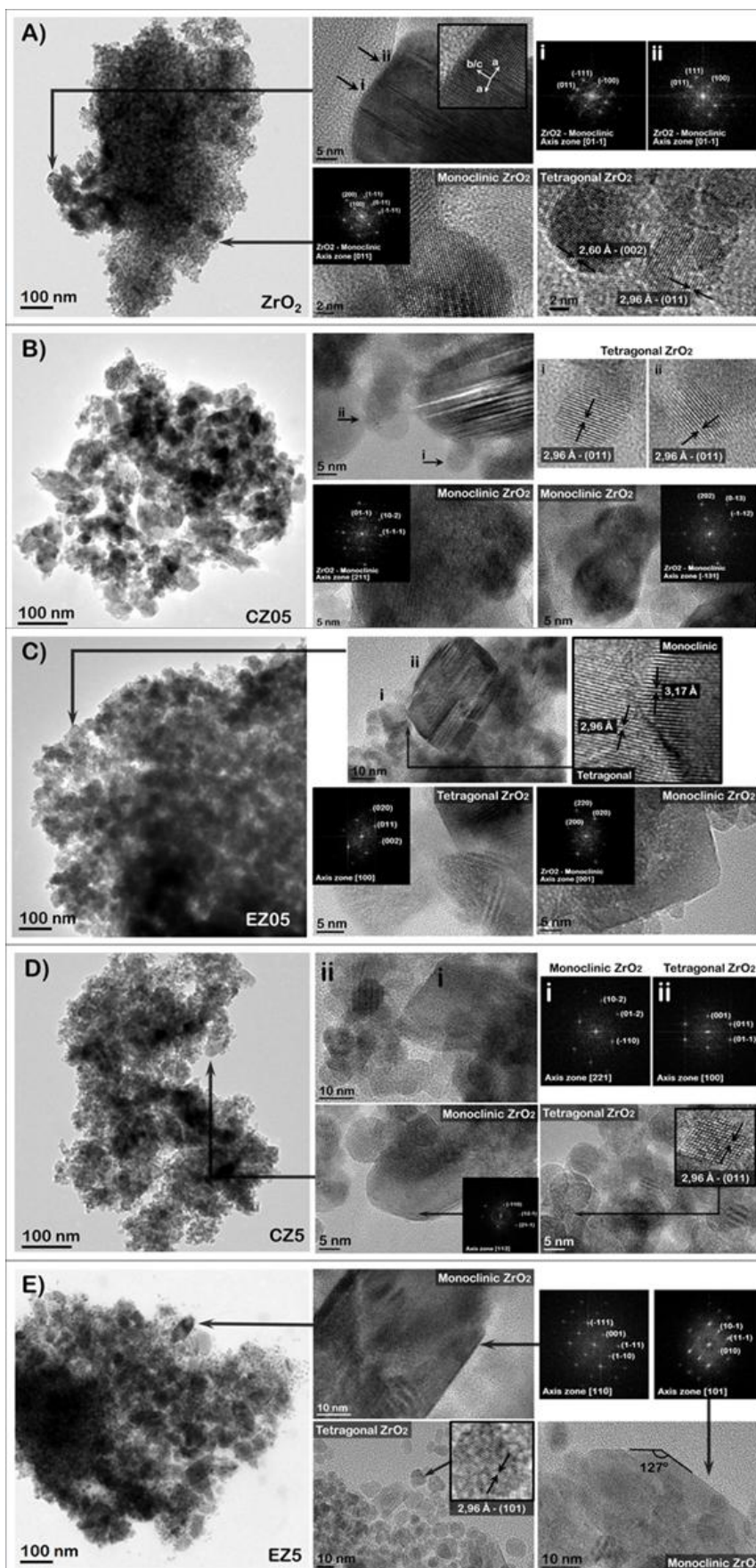
Figure 2. TEM (left column) and HR-TEM (center and right columns) images of pure ZrO₂ (A) and REO-doped samples, CZ05 (B), EZ05 (C), CZ5 (D) and EZ5 (E). For all samples the selected area electron diffraction (SAED) patterns are also presented.
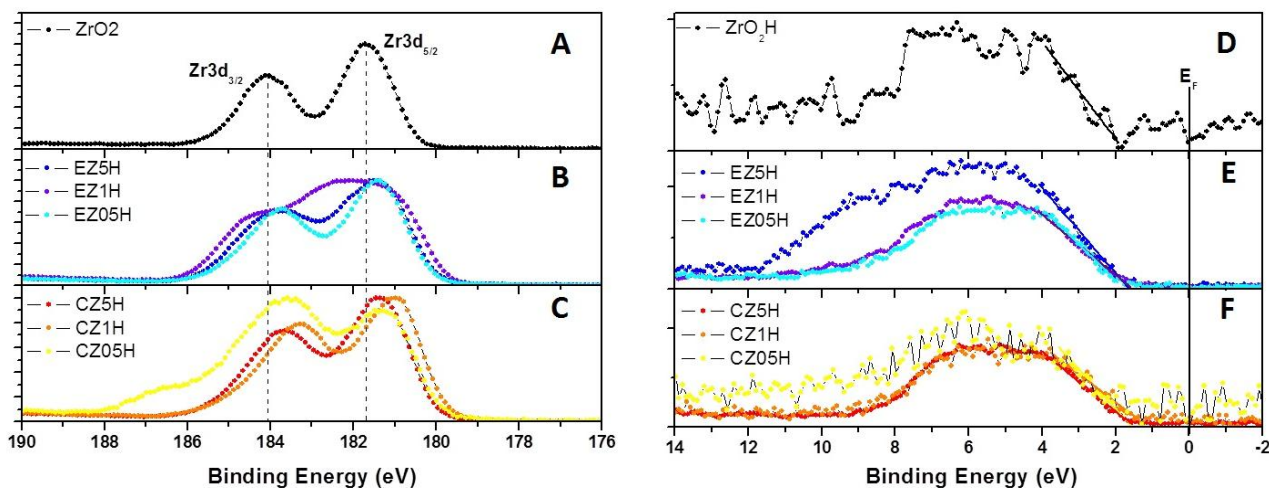
Figure 3. XPS Zr3d (A-C) and valence band region (D-E) high resolution spectra for the bare zirconia and the Er and Ce doped samples respectively.

In order to evaluate more in detail, the crystallographic aspect, the XPS spectra of the bare zirconia sample were compared with those of two ZrO_2 powders containing 100% monoclinic and tetragonal phases, respectively, as confirmed by XRD analyses and detailed in the supporting information (Figure S5). The Zr4p peak comparison is shown in the Figure S6 (SI). In agreement with previous literature reports [34], the tetragonal phase has a visible shift towards lower binding energy with respect to the monoclinic one. The signal here reported and assigned to the sample labelled as Z (pure zirconia) is overlapping quite well the monoclinic reference sample signal, which indicates the predominance of this crystalline phase as calculated by Rietveld refinement of XRD patterns (see Table 1).

Furthermore, the Er4d and Ce3d peaks were analyzed to evaluate the oxidation states of both dopants. In Figure S7-A the Er4d core level peak is shown for the EZ5 sample, with its deconvolution curve centered at 168.2 eV that is attributed to Er_2O_3 [35]. The Ce3d core level doublet is reported in Figure S7-B, together with the fitting curves, which have highlighted the presence of both Ce^{3+} and Ce^{4+} oxidation states [36]. To complete the XPS analysis, the attention was focused on the valence band region and the valence band maximum (VBM) energy level was calculated for each sample (Figure 3 D-F). According to the literature [37], a linear fit on the descending part of the signal towards the 0 eV value was made, which corresponds to the Fermi Energy (E_F) level. The distance between the x-intercept and the E_F corresponds to the VBM. The bare ZrO_2 has a VBM equal to (1.77 ± 0.11) eV, which is lower than other values reported in literature for zirconia thin films [38]. The Er-doped samples show VBM values similar to the Z sample one: 1.75 ± 0.01 eV (EZ05), 1.71 ± 0.04 eV (EZ1) and 1.77 ± 0.05 eV (EZ5). However, the shape of the curve envelope is quite different and more similar to that of an amorphous zirconium oxide valence band [33]. Moreover, the EZ5 sample possesses an enlargement towards the higher binding energy region, which is due to the presence of the Er4f peak, almost absent in the EZ05 and EZ1 samples, where the Er atomic concentration is lower. The Ce-doped samples show VB region spectra that are quite similar to that of an amorphous zirconium oxide, but with a relevant shift towards the lower binding energy region, which results in lower VBM values: 1.44 ± 0.03 eV (CZ05), 1.12 ± 0.04 eV (CZ1) and 1.51 ± 0.01 eV (CZ5). The VBM values obtained are reported in Table 2. The fact that the shape of the curve envelope changes towards that typical for the

9

amorphous ZrO_2 indicates, once again, that the insertion of dopants lowers the degree of crystallinity of the powders.

Table 2. Valence band maxima, energy gap, and photocatalytic performance: decoloration %, mineralization % and calculated kinetic rate (K_{app}) after 3 h of simulated sunlight irradiation.

Sample	VBM[a] [eV]	E_g[b] [eV]	Decoloration %	Mineralization%	K_{app} (10^{-2} / min)
Z	1.77 ± 0.11	5.15	23	8	0.09
EZ05	1.75 ± 0.01	5.13	88	27	1.03
EZ1	1.71 ± 0.04	5.13	71	17	0.58
EZ5	1.77 ± 0.05	5.12	88	43	0.91
CZ05	1.44 ± 0.03	4.06	92	44	1.45
CZ1	1.12 ± 0.04	3.84	81	27	0.73
CZ5	1.51 ± 0.01	3.55	81	43	0.79

[a] From XPS   [b] Calculated from the Tauc plot [39]

The influence of RE doping on the optical absorption of the various samples has been investigated by Diffuse Reflectance (DR) UV-Vis spectroscopy. Figure 4 compares the spectra recorded for pure zirconia with those of the variously doped samples (Ce, panel A and Er, panel B).

The addition of RE ions to ZrO_2 dramatically changes its optical properties. Indeed, the Ce doped ZrO_2 samples show an absorption shoulder progressively more intense according to the percentage of dopants, until it is possible to observe a real red shift of the absorption edge in the case of 5% cerium doping. This behavior, on the other hand, is not observed in the case Er doped ZrO_2, nevertheless the samples are colored thanks to the f-f transitions centered at the Er^{3+} ions, which result in a series of sharp absorption bands in the visible region [40]. As a matter of fact, increasing the RE ions content, the absorption in the visible region rises for both Ce and Er doped materials although through different mechanisms.
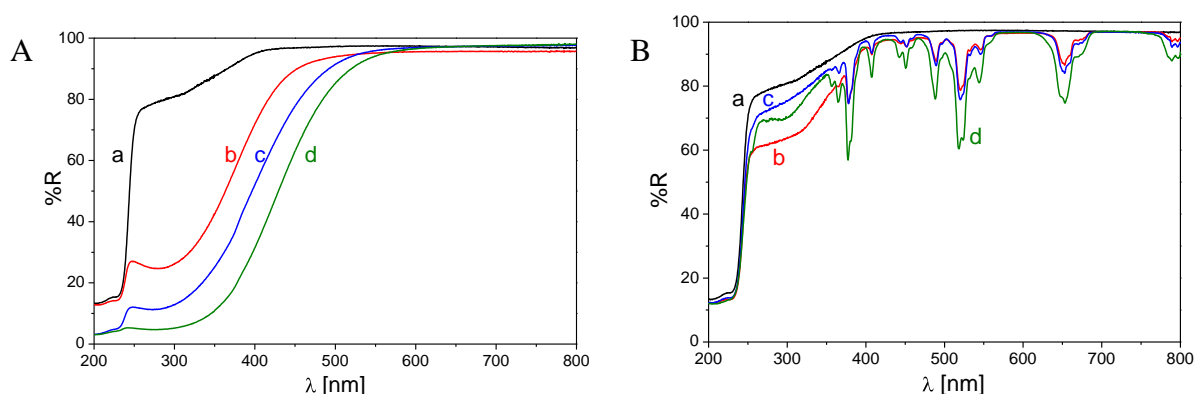

Figure 4. Diffuse reflectance absorbance spectra of pure ZrO_2 (a, black) and REO-doped ZrO_2 (panel A: REO=CeO_2, panel B: REO=Er_2O_3) with increasing concentration of REO dopant: 0.5%mol (b, red), 1%mol (c, blue), 5%mol (d, green).

3.2. Materials photoactivity

Electron Paramagnetic Resonance is a suitable technique to monitor the charge separation processes and the fate of the generated charge carriers. As shown by preliminary results from our group some photoactivity (i.e. charge separation) under visible light occurs in the case of Ce doped ZrO_2 material prepared via sol-gel. The effect of visible irradiation ($\lambda > 400$ nm, $h\nu < 3.1$ eV) was monitored in terms of a signal in the region at $g > 2.0$, typical of holes stabilized on oxygen ions (*i.e.* O^- ions) [22].
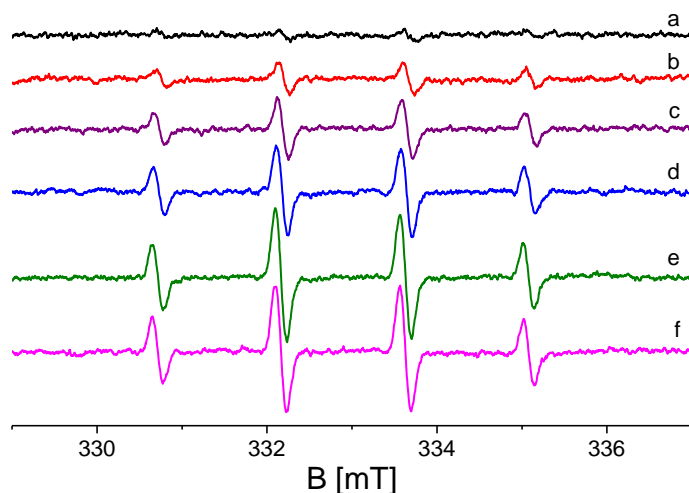

Figure 5. EPR spectra of the DMPO/OH• adduct produced by irradiation of an aqueous suspension of CZ5 with visible/NIR light (λ>400nm) as a function of the irradiation time: 0' (a, black), 5' (b, red), 15' (c, purple), 30' (d, blue), 60' (e, olive), 90' (f, magenta).

In this work, the photoactivity of the materials was tested under visible light irradiation, with a cut off filter at 400 nm, using DMPO (5,5-dimethyl-1-pyrroline-N-oxide) as spin trapping agent to detect the formation of hydroxyl radicals ($OH^\bullet$) in solution. The DMPO molecule forms with those radicals a stable paramagnetic adduct (DMPO/OH$^\bullet$), detectable with the EPR technique. The hydroxyl radicals are responsible for the oxidative degradation of organic molecules in photocatalytic reactions, and they are formed according to the following process:

$$h^+_{(VB)} + H_2O \rightarrow HO^\bullet + H^+ \tag{1}$$
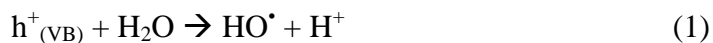
As expected, the pure ZrO_2 aqueous suspension does not form any radical under visible irradiation. Despite their color, also the Er doped ZrO_2 samples are inactive, while all the samples are active if irradiated with a wavelength including the UV-A region of radiation (results not reported for sake of brevity). On the other hand, all the Ce doped ZrO_2 materials can generate hydroxyl radicals also upon visible light irradiation, as it can be seen in Figure 5, where the spectra obtained for the CZ5 sample (the most active) are reported as a function of the irradiation time. All the spectra show the typical four lines of the DMPO/OH$^\bullet$ adduct and have been obtained by subtracting the spectrum relative to the irradiation of a DMPO solution used as a reference. The results are thus purely related to the presence of the powder suspension. The presence of the adduct is already appreciable after 5' of irradiation and reaches its maximum after 90'. The CZ05 and CZ1 materials showed similar activity, both being less active than the CZ5 sample (results not shown for sake of brevity).

11

The materials were then tested in the solar light driven photocatalytic degradation of Rhodamine B (RhB), a common textile dye. The absorbance spectrum of the as prepared RhB solution (Figure S8) exhibit a characteristic absorbance peak at 554 nm. Figure 6 A reports the obtained RhB disappearance curves in the presence of bare and RE doped ZrO_2. The adsorption of the dye on the samples' surface after one hour in dark is similar for all materials.
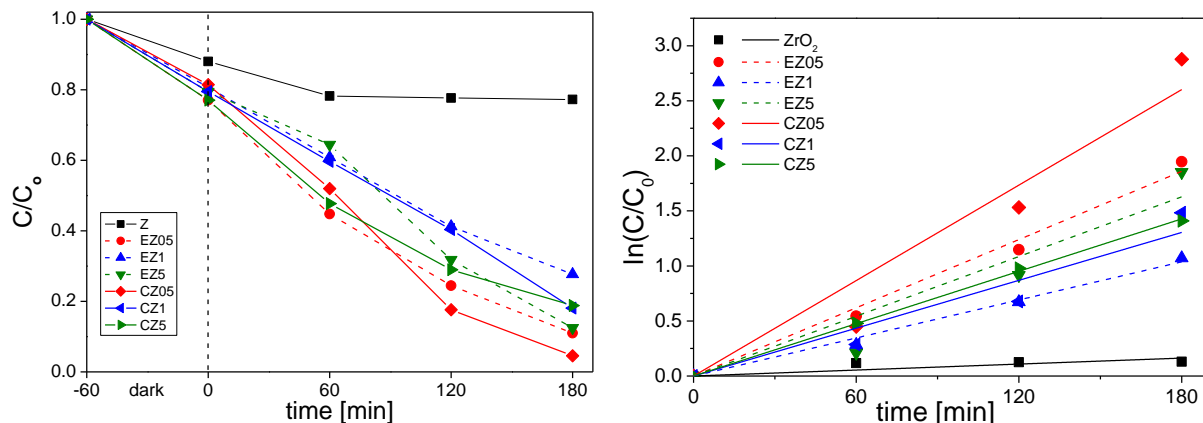

Figure 6. Panel A: RhB degradation curves in the presence of different catalysts under visible irradiation. Panel B: Kinetic curves for the different catalysts.

Nevertheless, when the irradiation starts, all the doped materials performed better than bare zirconia, which revealed that the induced optical transition in visible region enables photoexcitation and charge separation in the doped materials. The achieved results of decoloration and mineralization of *RhB* for bare and doped materials are given in Table. 2. Among the doped material the photocatalytic performance in decoloring *RhB* was slightly better in case of EZ05, EZ5 and CZ05 i.e. 88% for both EZ05, EZ5 samples and 92% in case of CZ05 after three hours. Figure 6 B reports the kinetic curves obtained for the various catalysts. The degradation curves approximate a pseudo-first-order reaction, thus the apparent rate constants, K_{app} can be calculated according to the equation:

$$K_{app} \, t = \ln (C/C_o) \qquad (2)$$

The calculated K_{app} for all the samples are reported in Table 2. For both Ce and Er dopants the maximum efficiency was reached with the lower amount of dopants, while the EZ1 sample was the one showing the lowest activity. These values indicate that all the prepared samples are able to absorb visible light and perform the photocatalytic degradation of *RhB*. The K_{app} of CZ05 sample, was found slightly higher than other doped samples i.e. 1.49×10^{-2} min^{-1}. However, the achieved mineralization (from the TOC analysis) evident that for all samples the mineralization is significantly lower than the decoloration (*e.g.* for CZ05 sample at 92% decoloration the achieved mineralization is only 44%). This suggests decoloration occurred first and then further degradation/mineralization followed, after the destabilization of the dye molecule, indicating that decoloration and degradation mechanisms are not simultaneous [41]. Indeed, it is known that the *RhB* photodegradation generates several intermediary products [42] and goes through the formation of triethylrhodamine, diethylrhodamine, ethylrhodamine and rhodamine having different λ_{max} at 555, 539, 522, 510, 498 nm, respectively. The degradation follow N-deethylation sensitization mechanism, initiated by self-sensitization of *RhB* in visible light followed by charge transport to the

12

photocatalyst and formation of active superoxide ions [43]. However, since in our experiments no additional or hypsochromic shift of absorbance peak was detected (see Figure S8), it can be assumed that *RhB* was degraded without intermediates, and this would be justified by using a visible lamp with a very low intensity that allowed to [41] avoid sensitization mechanisms.

4. Discussion

In the present paper, nanostructured samples of ZrO_2 were prepared and characterized, which present some visible light photoactivity when doped with rare earth elements (Ce and Er), with oxide-oxide concentration ratios of 0.5, 1 and 5% mol. The XRD and TEM analysis revealed that the RE elements are inserted in the ZrO_2 matrix, stabilizing with a little distortion the tetragonal polymorph. The EDS maps reported in the SI (Figure S4) show that the dopants are well dispersed in the matrix and no sign of RE oxides phases were detected in the micrographs nor in the XRD patterns. Coupling XPS and DRS analyses, it is possible to have some insight on the materials electronic structure. The valence band maximum (VBM) value obtained from XPS is indeed the distance between the VBM and the Fermi level (0 eV in the XPS experiment). The position of the bottom of the conduction band can be then obtained from the E_g value calculated with optical measurements. It is possible to see that neither the main energy gap nor the VBM value are highly affected by Er doping, resulting in electronic structures for the EZ materials that are very similar to that of pure ZrO_2. Interestingly for both the pure sample and the EZ samples the VBM value is lower than half of the E_g, which indicate that these materials behave as p-type semiconductors. This also indicates that some acceptor impurities may be also included in the matrix during the synthesis process. Interestingly for both the pure sample and the EZ samples the VBM value is lower than half of the E_g, which indicate that these materials behave as p-type semiconductors (Figure 7). This also indicates that some acceptor impurities may be also included in the matrix during the synthesis process. One possibility is the presence of interstitial oxygen in the monoclinic ZrO_2, which creates shallow traps near the valence band maximum [44]. The spin trapping results for these samples indicates that even if the insertion of Er brings to the absorption of visible light by the samples, the Er ions could act as recombination centers resulting in a lack of photoactivity when irradiated with visible light in aqueous suspension. Nevertheless, the samples resulted efficient in the degradation of RhB, where solar light was used. This suggests that the small fraction of UV light present in the halogen lamp emission spectrum was responsible for the materials photoactivity. The trend of efficiency of the materials EZ05>EZ5>EZ1) is indeed the same as the intensity of the absorption shoulder in the UV-region of the DR spectra and centered at 300 nm, due to zirconia defects.

In the case of Ce doped materials, the situation is quite different. Indeed, the insertion of cerium ions in the ZrO_2 matrix actually is responsible for the optical absorption in the visible region. This effect has already been reported in literature [22] and it has been explained by the insertion of Ce 4f levels in the middle of the zirconia energy gap forming unoccupied energy levels, available for the photoexcited electrons. Also in this case, the VBM value is lower than half of the energy gap indicating a p-type character for the materials, more pronounced for the CZ1 sample than for the CZ05 and CZ5 samples, the last one is indeed the sample with the Fermi energy level closest to the intrinsic one (which would be half of the energy gap). The modified band gap for the CZ materials enhances the visible light photocatalytic activity confirmed by both the spin trapping technique and

the photodegradation of *RhB*. The higher position of the valence band maximum for the CZ1 sample with respect to the others (CZ05 and CZ5) can be responsible for the lower mineralization achieved by this sample, since it corresponds to a lower oxidation chemical potential.

In general, the here reported photocatalytic and spin trapping results confirm that the mechanism of RhB degradation by the RE doped-ZrO_2 samples under light is mainly driven by the formation of $OH^{\bullet}$ radicals (which is favored by the p-type behavior of the samples) that attack the dye molecule and cause its mineralization, without a dye-sensitization effect.

5. Conclusions

In this work, nanostructured rare earth, RE-doped zirconia samples were successfully synthesized through a simple hydrothermal method, with a CeO_2 or Er_2O_3-based contents varying from 0.5 to 5% molar. The samples were characterized by using several techniques, such as XRD, TEM, XPS, DR UV-Vis spectroscopy. The structural characterization techniques evidenced that all the samples were constituted by a mixture of tetragonal and monoclinic zirconia, containing both nanocrystals and large flat grains. The addition of RE in the structure stabilized the nanocrystalline form and the tetragonal phase of zirconia. All the doped samples resulted able to absorb visible light. The addition of Ce creates new states inside the band gap, producing a red shift of the materials' absorption edge, while the f-f internal transitions of the Er^{3+} ions were responsible for the pink color of the Er doped materials, which did not show a fundamental edge shift.

The photoactivity of the materials under visible light irradiation was tested using DMPO as spin trapping agent to detect the formation of hydroxyl radicals ($OH^{\bullet}$) in solution. The Ce doped samples resulted able to generate this kind of radicals that are responsible for the oxidation of several organic pollutants. On the other hand, neither pure zirconia nor the Er doped samples were able to achieve the same results.

Finally, the materials were tested for the photodegradation of the Rhodamine B dye under irradiation with a simulated solar source (halogen lamp). All the doped materials, both Ce and Er, resulted active in the degradation of the dye producing a decoloration as high as 92% in three hours. We concluded that the small presence of UV-A light in the solar spectrum was responsible for the increased activity of Er doped samples, while according to the spin trapping results the Ce doped samples are able to exploit visible light for the dye degradation. These results confirm that the insertion of RE ions in wide band gap materials is a good strategy for the design of materials that can be employed in water remediation from organic pollutants.

6. Acknowledgements

7.Declaration of interest

Declarations of interest: none.

8. References:

[1] Commission staff working document. Impact assesment. Accompanying the document: Communication from the Commission to the European Parliament, the Council, the European Economic and Social Committee and the Committee of the Regions; A policy framework for climate and energy in the period from 2020 up to 2030., EUROPEAN COMMISSION.

[2] K.E. O'Shea, D.D. Dionysiou, Advanced Oxidation Processes for Water Treatment, J. Phys. Chem. Lett. 3(15) (2012) 2112-2113.

[3] I.K. Konstantinou, T.A. Albanis, TiO_2-assisted photocatalytic degradation of azo dyes in aqueous solution: kinetic and mechanistic investigations: A review, Appl. Catal., B 49(1) (2004) 1-14.

[4] M.R. Hoffmann, S.T. Martin, W. Choi, D.W. Bahnemann, Environmental applications of semiconductor photocatalysis, Chem. Rev. 95(1) (1995) 69–96.

[5] A. Fujishima, K. Honda, Electrochemical Photolysis of Water at a Semiconductor Electrode, Nature 238(5358) (1972) 37-38.

[6] A.V. Emeline, V.N. Kuznetsov, V.K. Ryabchuk, N. Serpone, On the way to the creation of next generation photoactive materials, Environ. Sci. Pollut. Res. 19(9) (2012) 3666-3675.

[7] N. Serpone, A.V. Emeline, Semiconductor Photocatalysis — Past, Present, and Future Outlook, J. Phys. Chem. Lett. 3(5) (2012) 673-677.

[8] C. Martinez Suarez, S. Hernández, N. Russo, $BiVO_4$ as photocatalyst for solar fuels production through water splitting: A short review, Appl. Catal., A 504 (2015) 158-170.

[9] X. Liu, F. Wang, Q. Wang, Nanostructure-based WO_3 photoanodes for photoelectrochemical water splitting, Phys. Chem. Chem. Phys. 14(22) (2012) 7894-7911.

[10] Y. Inoue, Effects of Metal-Ion Doping, Removal and Exchange on Photocatalytic Activity of Metal Oxides and Nitrides for Overall Water Splitting, On Solar Hydrogen & Nanotechnology, John Wiley & Sons, Ltd2010, pp. 559-588.

[11] D. Hidalgo, S. Bocchini, M. Fontana, G. Saracco, S. Hernandez, Green and low-cost synthesis of PANI-TiO_2 nanocomposite mesoporous films for photoelectrochemical water splitting, RSC Adv. 5(61) (2015) 49429-49438.

[12] S. Hernandez, D. Hidalgo, A. Sacco, A. Chiodoni, A. Lamberti, V. Cauda, E. Tresso, G. Saracco, Comparison of photocatalytic and transport properties of TiO_2 and ZnO nanostructures for solar-driven water splitting, Phys. Chem. Chem. Phys. 17(12) (2015) 7775-7786.

[13] A. Wolcott, J.Z. Zhang, Multidimensional Nanostructures for Solar Water Splitting: Synthesis, Properties, and Applications, On Solar Hydrogen & Nanotechnology, John Wiley & Sons, Ltd2010, pp. 459-505.

[14] S. Fernandez-Garcia, L. Jiang, M. Tinoco, A.B. Hungria, J. Han, G. Blanco, J.J. Calvino, X.W. Chen, Enhanced Hydroxyl Radical Scavenging Activity by Doping Lanthanum in Ceria Nanocubes, J. Phys. Chem. C 120(3) (2016) 1891-1901.

[15] Y. Xue, Q.F. Luan, D. Yang, X. Yao, K.B. Zhou, Direct Evidence for Hydroxyl Radical Scavenging Activity of Cerium Oxide Nanoparticles, J. Phys. Chem. C 115(11) (2011) 4433-4438.

[16] S.Y. Hao, J. Hou, P. Aprea, F. Pepe, Mesoporous Ce-Pr-O solid solution with efficient photocatalytic activity under weak daylight irradiation, Applied Catalysis B-Environmental 160 (2014) 566-573.

[17] S.N. Basahel, T.T. Ali, M. Mokhtar, K. Narasimharao, Influence of crystal structure of nanosized ZrO_2 on photocatalytic degradation of methyl orange, Nanoscale Res. Lett. 10(1) (2015) 1-13.

[18] W. Jiang, J. He, J. Zhong, J. Lu, S. Yuan, B. Liang, Preparation and photocatalytic performance of ZrO_2 nanotubes fabricated with anodization process, Appl. Surf. Sci. 307 (2014) 407-413.

[19] S. Kumar, A.K. Ojha, Oxygen vacancy induced photoluminescence properties and enhanced photocatalytic activity of ferromagnetic ZrO_2 nanostructures on methylene blue dye under ultra-violet radiation, J. Alloys Compd. 644 (2015) 654-662.

[20] Y. Kohno, T. Tanaka, T. Funabiki, S. Yoshida, Identification and reactivity of a surface intermediate in the photoreduction of CO_2 with H_2 over ZrO_2, J. Chem. Soc., Faraday Trans. 94(13) (1998) 1875-1880.

[21] A.N. Bugrov, I.A. Rodionov, I.A. Zvereva, R.Y. Smyslov, O.V. Almjasheva, Photocatalytic activity and luminescent properties of Y, Eu, Tb, Sm and Er-doped ZrO_2 nanoparticles obtained by hydrothermal method, Int. J. Nanotechnol. 13(1-3) (2016) 147-157.

[22] C. Gionco, M.C. Paganini, E. Giamello, R. Burgess, C. Di Valentin, G. Pacchioni, Cerium-Doped Zirconium Dioxide, a Visible-Light-Sensitive Photoactive Material of Third Generation, J. Phys. Chem. Lett. 5 (2014) 447-451.

[23] C. Gionco, M.C. Paganini, M. Chiesa, S. Maurelli, S. Livraghi, E. Giamello, Cerium doped zirconium dioxide as a potential new photocatalytic material. The role of the preparation method on the properties of the material, Appl. Catal., A 504 (2015) 338-343.

[24] S.G. Botta, J.A. Navio, M.C. Hidalgo, G.M. Restrepo, M.I. Litter, Photocatalytic properties of ZrO_2 and Fe/ZrO_2 semiconductors prepared by a sol-gel technique, J. Photochem. Photobiol., A 129 (1999).

[25] G. Poungchan, B. Ksapabutr, M. Panapoy, One-step synthesis of flower-like carbon-doped ZrO_2 for visible-light-responsive photocatalyst, Mater. Des. 89 (2016) 137-145.

[26] H. Sudrajat, S. Babel, H. Sakai, S. Takizawa, Rapid enhanced photocatalytic degradation of dyes using novel N-doped ZrO_2, J. Environ. Manage. 165 (2016) 224-234.

[27] L. Lutterotti, Total pattern fitting for the combined size-strain-stress-texture determination in thin film diffraction, Nucl. Instrum. Methods Phys. Res., Sect. B 268(3-4) (2010) 334-340.

[28] D. Balzar, N. Audebrand, M.R. Daymond, A. Fitch, A. Hewat, J.I. Langford, A. Le Bail, D. Louër, O. Masson, C.N. McCowan, N.C. Popa, P.W. Stephens, B.H. Toby, Size–strain line-broadening analysis of the ceria round-robin sample, J. Appl. Crystallogr. 37(6) (2004) 911-924.

[29] A. Galtayries, R. Sporken, J. Riga, G. Blanchard, R. Caudano, XPS comparative study of ceria/zirconia mixed oxides: powders and thin film characterisation, J. Electron. Spectrosc. Relat. Phenom. 88 (1998) 951-956.

[30] D. Majumdar, D. Chatterjee, X-Ray Photoelectron Spectroscopic Studies on Yttria, Zirconia, and Yttria-Stabilized Zirconia, J. Appl. Phys. 70(2) (1991) 988-992.

[31] A. Barrera, J.A. Montoya, P. del Angel, J. Navarrete, M.E. Cano, F. Tzompantzi, A. Lopez-Gaona, Surface properties of palladium catalysts supported on ternary ZrO_2-Al_2O_3-WO_x oxides prepared by the sol-gel method: Study of the chemical state of the support, J. Phys. Chem. Solids 73(8) (2012) 1017-1025.

[32] S. Ardizzone, M.G. Cattania, P. Lazzari, P. Lugo, Hydrothermal Route to Pure Phase ZrO_2 - Interfacial Reactivity by XPS and Electrochemical Determinations, Colloids Surf., A 90(1) (1994) 45-54.

[33] G. Bakradze, L.P.H. Jeurgens, E.J. Mittemeijer, Valence-Band and Chemical-State Analyses of Zr and O in Thermally Grown Thin Zirconium-Oxide Films: An XPS Study, J. Phys. Chem. C 115(40) (2011) 19841-19848.

[34] L.K. Dash, N. Vast, P. Baranek, M.C. Cheynet, L. Reining, Electronic structure and electron energy-loss spectroscopy of ZrO_2 zirconia, Phys. Rev. B 70(24) (2004) 17.

[35] N. Guerfi, O. Bourbia, S. Achour, Study of erbium oxidation by XPS and UPS, in: A. MendezVilas (Ed.), Cross-Disciplinary Applied Research in Materials Science and Technology, Trans Tech Publications Ltd, Durnten-Zurich, 2005, pp. 193-196.

[36] C.J. Zhang, M.E. Grass, A.H. McDaniel, S.C. DeCaluwe, F. El Gabaly, Z. Liu, K.F. McCarty, R.L. Farrow, M.A. Linne, Z. Hussain, G.S. Jackson, H. Bluhm, B.W. Eichhorn, Measuring fundamental properties in operating solid oxide electrochemical cells by using in situ X-ray photoelectron spectroscopy, Nat. Mater. 9(11) (2010) 944-949.

[37] V. Gritsenko, D. Gritsenko, S. Shaimeev, V. Aliev, K. Nasyrov, S. Erenburg, V. Tapilin, H. Wong, M.C. Poon, J.H. Lee, J.W. Lee, C.W. Kim, Atomic and electronic structures of amorphous ZrO_2 and HfO_2 films, Microelectron. Eng. 81(2-4) (2005) 524-529.

[38] Y.H. Wong, K.Y. Cheong, Band alignment and enhanced breakdown field of simultaneously oxidized and nitrided Zr film on Si, Nanoscale Res. Lett. 6 (2011) 5.

[39] C. Gionco, M.C. Paganini, E. Giamello, O. Sacco, V. Vaiano, D. Sannino, Rare earth oxides in zirconium dioxide: How to turn a wide band gap metal oxide into a visible light active photocatalyst, J. Energy Chem. 26(2) (2017) 270-276.

[40] W.T. Carnall, P.R. Fields, K. Rajnak, Electronic energy levels in the trivalent lanthanide aquo ions. I. Pr^{3+}, Nd^{3+}, Pm^{3+}, Sm^{3+}, Dy^{3+}, Ho^{3+}, Er^{3+}, and Tm^{3+}, J. Chem. Phys. 49(10) (1968) 4403-4406.

[41] D. Sánchez-Martínez, I. Juárez-Ramírez, L.M. Torres-Martínez, I. De León-Abarte, Photocatalytic properties of Bi_2O_3 powders obtained by an ultrasound-assisted precipitation method, Ceram. Int. 42(1) (2016) 2013-2020.

[42] Z. He, C. Sun, S. Yang, Y. Ding, H. He, Z. Wang, Photocatalytic degradation of rhodamine B by Bi(2)WO(6) with electron accepting agent under microwave irradiation: mechanism and pathway, J Hazard Mater 162(2-3) (2009) 1477-86.

[43] M. Rochkind, S. Pasternak, Y. Paz, Using dyes for evaluating photocatalytic properties: A critical review, Molecules 20(1) (2015) 88-110.

[44] A.S. Foster, V.B. Sulimov, F. Lopez Gejo, A.L. Shluger, R.M. Nieminen, Structure and electrical levels of point defects in monoclinic zirconia, Phys. Rev. B 64(22) (2001) 224108.